



Published in final edited form as:

Neuroimage. 2017 April 15; 150: 162–176. doi:10.1016/j.neuroimage.2017.02.002.

High b-value and high Resolution Integrated Diffusion (HIBRID) imaging

Qiuyun Fan¹, Aapo Nummenmaa¹, Jonathan R. Polimeni^{1,2}, Thomas Witzel¹, Susie Y. Huang¹, Van J. Wedeen¹, Bruce R. Rosen^{1,2}, and Lawrence L. Wald^{1,2,*}

¹Athinoula A. Martinos Center for Biomedical Imaging, Department of Radiology, Harvard Medical School, Massachusetts General Hospital, Charlestown, MA, USA

²Harvard-MIT Division of Health Sciences and Technology, Massachusetts Institute of Technology, Cambridge, MA, USA

Abstract

The parameter selection for diffusion MRI experiments is dominated by the “k-q tradeoff” whereby the Signal to Noise Ratio (SNR) of the images is traded for either high spatial resolution (determined by the maximum k value collected) or high diffusion sensitivity (effected by b value or the q vector) but usually not both. Furthermore, different brain regions (such as gray matter and white matter) likely require different tradeoffs between these parameters due to the size of the structures to be visualized or the length-scale of the microstructure being probed. In this case, it might be advantageous to combine information from two scans – a scan with high q but low k (high angular resolution in diffusion but low spatial resolution in the image domain) to provide maximal information about white matter fiber crossing, and one low q but high k (low angular resolution but high spatial resolution) for probing the cortex.

In this study, we propose a method, termed High b-value and high Resolution Integrated Diffusion (HIBRID) imaging, for acquiring and combining the information from these two complementary types of scan with the goal of studying diffusion in the cortex without compromising white matter fiber information. The white-gray boundary and pial surface obtained from anatomical scans are incorporated as prior information to guide the fusion. We study the complementary advantages of the fused datasets, and assess the quality of the HIBRID data compared to either alone.

Keywords

Brain connectivity; Human Connectome Project (HCP); multi-shell multi-resolution MRI; high resolution; HARDI; crossing fiber

*Corresponding author at: Athinoula A. Martinos Center for Biomedical Imaging 149 13th Street, Charlestown, MA, 02129, USA. Tel.: +1 617 724 9706; fax: +1 617 726 7422. wald@nmr.mgh.harvard.edu.

Publisher's Disclaimer: This is a PDF file of an unedited manuscript that has been accepted for publication. As a service to our customers we are providing this early version of the manuscript. The manuscript will undergo copyediting, typesetting, and review of the resulting proof before it is published in its final citable form. Please note that during the production process errors may be discovered which could affect the content, and all legal disclaimers that apply to the journal pertain.

1. Introduction

Broadly speaking, conventional High Angular Resolution Diffusion Imaging (HARDI) style imaging studies of the brain make a tradeoff between the image resolution and the diffusion encoding, since increasing either comes at a cost in image Signal to Noise Ratio (SNR). We refer to this tradeoff as the k-q tradeoff. A high-k examination would use high resolution in the image space, likely at the expense of diffusion weighting, while a high-q examination would use a high b-value for increased angular resolution of white-matter fibers. Trying to do both in the same examination would lead to insufficient image SNR.

Despite that both high-k and high-q are desired imaging capabilities, they are not always equally needed for different anatomical structures in the brain. For example, the major white matter (WM) fiber bundles in the brain consist of axons which are coherently aligned along the bundle and thus relatively smooth spatially. The challenges for tracking them lie in the regions where they cross other tracts, such as in the centrum semiovale (Jeurissen et al., 2013). A number of HARDI methods (Anderson, 2005; Tournier et al., 2004; Tuch et al., 2002) have been developed to address these crossings, and high b-value data have been shown to help resolve the individual fiber orientations (Fan et al., 2014; Fan et al., 2016; White and Dale, 2009).

In contrast, cerebral cortex is relatively thin (2–3 mm) and extensively folded into gyral and sulcal patterns. Intra-cortical axonal fibers are primarily radial to the cortical surface, which has been widely seen in optical imaging studies [see Magnain et al. (Magnain et al., 2014b) and Zilles et al. (Zilles et al., 2016) for examples]. The same phenomenon was also reported in recent diffusion MRI (dMRI) studies in ex vivo animal brains (Reveley et al., 2015), ex vivo human brains (McNab et al., 2009; Miller et al., 2011), as well as in vivo human brains (Heidemann et al., 2012; Kleinnijenhuis et al., 2015; McNab et al., 2013b; Song et al., 2014). At the intersection between cerebral gray matter (GM) and the underlying WM, pericortical axonal fibers take sharp turns when branching off from their bundles and bend abruptly to align radially to the cortical ribbon. These finer details of intra-cortical and pericortical axonal fibers will heavily rely upon high imaging resolution to be resolved.

In this study, we propose the High b-value and high Resolution Integrated Diffusion (HIBRID) imaging method¹. Instead of picking one k-q balance that is a compromise for both WM and GM, we acquired two complementary datasets, each of which pushes to the limit of either k- or q-space sampling by compromising the other.

In the similar spirit, the RubiX (Resolutions Unified for Bayesian Inference of Xings) method (Sotiropoulos et al., 2013) models single-shell signal of a high resolution (1.5 mm) scan and a high SNR scan (3.0 mm) to improve local fiber orientation estimates, where some imaging parameters (i.e., TR/TE, echo spacing, etc.) need to be kept the same in order to model the MR signal explicitly. More recently, the model has been extended (Sotiropoulos et al., 2016) to allow joint analysis of HCP datasets of different spatial resolutions (1.25 mm and 1.05 mm) and b-values (up to 3000 and 2000 s/mm²) that are acquired on multiple

¹The acronym of HIBRID sounds similar to the name of Hybrid Diffusion Imaging (HYDI) (Wu, Y.C., Alexander, A.L., 2007. Hybrid diffusion imaging. *Neuroimage* 36, 617–629.), which is a distinct technique. We would like to make a note to avoid confusions.

platforms (3T and 7T). Although the spatial resolution and b-values of the two datasets are not remarkably different, the joint analysis was shown to gain complementary spatial and angular information from the two datasets to benefit the fiber orientation estimates in both white matter and gray matter.

Our approach proposes to sample a larger range of k- and q-space. We study the advantages and limitations inherent to each of the complementary datasets, and aim to provide the best informative data for local fiber orientation estimates given what imaging capabilities (k- or q-) are most needed for the local structures. Half of the high k- and half of the high q- datasets were used to generate the HIBRID data so that the total acquisition time is approximately matched with the high k- and high q-datasets standing alone. We assessed the quality of the HIBRID data obtained, explored its potential significance in improving diffusion tractography, and discussed the rationale of the method and intriguing ideas for future investigations.

2. Materials and Methods

2.1. Data Acquisition

Data were acquired from four healthy adult subjects on the 3T MGH-USC Connectome Scanner (MAGNETOM Skyra CONNECTOM, Siemens Healthcare), using a gradient system that is capable of generating up to 300 mT/m gradient strength (McNab et al., 2013a; Setsompop et al., 2013). A custom-made 64-channel head coil (Keil et al., 2013) was used for signal reception. All participants gave written informed consent, and the experiments were carried out with approval from the institutional review board of Partners Healthcare.

A spin-echo Echo Planar Imaging (EPI) sequence was used to acquire diffusion weighted (DW) MRI data. A high b-value dataset was acquired with $b = 8000 \text{ s/mm}^2$ and 2 mm isotropic voxel size (the 2.0 mm, $b=8\text{k}$ dataset), $TR/TE = 3000/60 \text{ ms}$, $G_{\max} = 200\text{mT/m}$, where 120 DW directions were sampled. A high resolution dataset was acquired with $b = 1500 \text{ s/mm}^2$ and 1 mm isotropic voxel size (the 1.0 mm, $b=1.5\text{k}$ dataset), $TR/TE = 6700/69 \text{ ms}$, where 60 DW directions were sampled. Both datasets were acquired twice: one with the phase encoding (PE) direction along $R \gg L$ and the other with PE direction along $L \gg R$ to allow corrections of geometric distortions (Andersson and Sotiropoulos, 2016). The field of view (FOV) = $180 \times 164 \text{ mm}$ ($AP \times RL$), nominal echo spacing = 0.95 ms, partial Fourier factor = 7/8 for both acquisitions. The echo spacing and the FOV along the PE direction were set to be the same in the two datasets, to keep the EPI geometric distortions identical, yielding a maximum readout gradient strength of 31.05 mT/m and 14.38 mT/m for the 1.0mm, $b=1.5\text{k}$ and 2.0mm, $b=8\text{k}$ datasets respectively. A Generalized Autocalibrating Partially Parallel Acquisition (GRAPPA) factor of 3 was used for in-plane acceleration, along with a blipped-CAIPI simultaneous multi-slice/multiband (Feinberg et al., 2010; Feinberg and Setsompop, 2013; Larkman et al., 2001; Setsompop et al., 2012a; Setsompop et al., 2012b) factor of 2 for slice acceleration (CAIPI FOV shift factor = 2), for both acquisitions. A Fast Low angle Excitation Echo Train (FLEET) technique (Polimeni et al., 2015) was used to suppress GRAPPA reconstruction artifacts due to breathing and head motions during the Auto-Calibration Signal (ACS) acquisition.

Four $b \approx 0$ images were acquired at the beginning of the scan, and, thereafter, one $b \approx 0$ image was interspersed at every 12 DW images, yielding eight $b \approx 0$ images per 60 DW images. The total acquisition time for the diffusion MRI scans was approximately 36 mins, where about 17 mins was spent on the 2.0 mm, $b=8k$ dataset and about 19 mins on the 1.0 mm, $b=1.5k$ dataset. A Multi-Echo Magnetization-Prepared Rapid Acquisition Gradient Echo (MEMPRAGE) (van der Kouwe et al., 2008) image was also acquired ($T_{acq} \approx 6$ mins) to provide an anatomical reference. The MEMPRAGE parameters are: matrix and FOV (read, phase, partition) = $256 \times 256 \times 176$, $256 \times 256 \times 176$, TI/TR/TE/flip = 1100 ms/2530 ms/1.15, 3.03, 4.89, 6.75 ms/7 degrees, readout BW = 651 Hz/pixel.

Two additional datasets were acquired in one of the 4 subjects to assess the the influence of spatial resolution at matched b -value of 1500 s/mm^2 ; one with 1.5 mm and one with 2.0 mm isotropic resolution. For these two additional datasets, the TR/TE was 4000/56 ms and 4000/51 ms, respectively. Acquisition time was approximately 12 minutes for each resolution.

2.2. Data Processing

All images were corrected for gradient nonlinearity. For diffusion MRI data, the interspersed $b \approx 0$ images with reversed PE directions were used to correct for susceptibility distortions. With all the $b \approx 0$ images, a field map was estimated using the TOPUP tool (Andersson et al., 2003) in the FSL package (Jenkinson et al., 2012; Smith et al., 2004). The TOPUP tool also estimated bulk head motions between the $b \approx 0$ images. The field maps were then used to correct for susceptibility distortions in the DW images, where the DW data were divided into groups, each starting with an interspersed $b \approx 0$ image, and the unwarping was applied to each pair of data groups which were acquired with identical DW encoding but reversed PE directions, using ‘applytopup’. We found it helps to improve the tolerance to head motion that occurred between interleaved $b \approx 0$ images, by grouping the DW data and apply susceptibility unwarping with the corresponding head motion estimates. Thus, each pair of DW datasets with identical DW encoding but reversed PE directions yields one DW dataset after the TOPUP step.

The average $b \approx 0$ image of the 2.0 mm, $b=8k$ dataset was registered to the average $b \approx 0$ image of the 1.0 mm, $b=1.5k$ dataset, using the Boundary Based Registration tool (bbrregister) (Greve and Fischl, 2009) in the FreeSurfer package V5.3.0 (Fischl, 2012) with 6 degrees of freedom (DOF). The transformation was then applied to the entire 2.0 mm, $b=8k$ dataset with the spline interpolation using the 1.0mm $b \approx 0$ image as a reference volume, and thus yielding an up-sampled high- b dataset with a 1.0 mm voxel size. The rotation component of the transformation was extracted and used to rotate b -vectors of the 2.0 mm, $b=8k$ dataset accordingly. The two datasets were then concatenated prior to eddy current correction for a joint eddy current correction using EDDY (Andersson and Sotiropoulos, 2016). A joint modeling of multi-shell data was found to result better corrections, likely because the Gaussian process is able to make use of the information from one shell when making predictions about another shell (Andersson and Sotiropoulos, 2016).

To match for scan time, we used only the R>>L phase encoded images to generate the HIBRID datasets ($T_{acq} \approx 18$ mins), so that half of high k - and high q -datasets were used,

without undersampling the diffusion directions. The preprocessing for this dataset is identical to the procedures above, except that only the R>>L phase encoded data were used in the step of ‘applytopup’.

The preprocessing for the spatial resolution comparison with matched b-value (1500 s/mm²) was performed differently. To avoid confounds from smoothing during interpolations and resampling, the corrections were performed separately in their native spatial resolutions. The TOPUP results were not applied to images but were saved and used as input to eddy. Then, the susceptibility, motion and eddy current corrections were corrected in one step (<http://fsl.fmrib.ox.ac.uk/fsl/fslwiki/eddy/UsersGuide>).

2.3. Data Analyses

“Laminar” cortical depth analysis—The MEMPRAGE data was input to FreeSurfer for an automatic cortical surface reconstruction and anatomical parcellation, which calculates the pial and white-gray boundary (WGB) surfaces (Dale et al., 1999; Fischl et al., 1999). Intermediate surfaces between the pial surface and the WGB were generated at intervals of 20% of cortical thickness (Polimeni et al., 2010). An additional surface was created inside the WM at a depth of 20% of the cortical thickness below the WGB. Therefore, 7 surfaces were generated in total: pial, WGB, 4 intermediate surfaces within cortical GM, and the surface inside the WM.

The average of the $b \approx 0$ images from the 1.0 mm, $b=1.5k$ dataset after susceptibility correction was registered to the T1w MEMPRAGE image using the Boundary Based Registration tool in FreeSurfer with 6 DOF to account for head movements, which comprises of translational and rotational components. The inverse transformation was used to calculate the coordinates of the surface meshes in the DW EPI image space. The local primary diffusion direction (PDD, i.e., the primary eigenvector of diffusion tensor) was sampled at every vertex on the surfaces, using the trilinear interpolation. Since the polarity of the PDD is physically meaningless (i.e., $[0\ 0\ 1]$ is identical to $[0\ 0\ -1]$), when performing the interpolation, the PDDs in the neighborhood were assigned the polarity that places it in maximal alignment with the local surface normal (i.e., so its angle w.r.t. surface normal is $<90^\circ$ angle, otherwise signs will be flipped). The radially was then defined as the dot product of the PDD at each vertex and the surface normal (McNab et al., 2013b), so that a radiality value of 1 indicates the PDD is locally radial to the given cortical surface, and a radiality value of 0 indicates it is locally tangential to the surface. The radiality indices were measured at the location of all 7 surfaces, and were compared between the 1.0 mm, $b=1.5k$ dataset and the 2.0 mm, $b=8k$ dataset.

For the comparison where b-value was fixed and voxel size was varied, the vertices of the surface mesh were further divided into three groups based on their local mean curvature (H) on the WGB surface: (i) $H < -0.15\text{ mm}^{-1}$ for gyral crowns; (ii) $|H| \leq 0.15\text{ mm}^{-1}$ for sulcal walls; and (iii) $H > 0.15\text{ mm}^{-1}$ for sulcal fundi, similar to previous analyses (McNab et al., 2013b).

HARDI characteristics of two datasets—q-ball ODFs (Descoteaux et al., 2007) were reconstructed for the two datasets. For the 2.0 mm, $b=8k$ dataset, a maximum Spherical

Harmonic order (L_{\max}) of 10 with a Laplace-Beltrami regularization parameter (λ) of 0.001 yields a good balance between preserving high frequency components in ODF without severely sacrificing stability (see results of Jackknife resampling below). For the 1.0 mm, b=1.5k dataset, a regularization of $\lambda = 0.006$ was used, and L_{\max} was lowered to 4 to reflect the modest degree of diffusion weighting in the data (i.e., lower b-value). The ODF calculation used here neglects solid angle correction, which will cause some degree of artificial blurring. The calculation of the correction factor usually relies upon an approximation of mono-exponential signal decay (Aganj et al., 2010; Tristan-Vega et al., 2009), which is less appropriate for higher b-values. For this reason, we stick to the more widely used ODF calculation in the current work.

High-b and high-resolution diffusion data integration—The fusion of the two datasets was performed on the ODFs themselves. Explicitly, a HIBRID ODF was calculated as the weighted sum of the ODFs obtained from the two datasets separately. The weights were calculated as follows.

The global normalization: Before fusing the data, the ODFs were globally normalized between the two datasets. The global normalization factor was determined by comparing the histograms of the amplitudes of the largest peaks in the ODFs. The histograms were obtained from voxels within a 2 mm distance from the WGB. The chosen scale factor minimized the L_2 -norm difference between the histograms. This forces the ODF peak amplitudes of the two datasets to match near the WGB.

We prefer the global normalization to the voxel-wise min-max normalization because in tissue with low anisotropy (such as CSF or subcortical GM), a min-max normalization will impose a larger amplification factor than the highly anisotropic voxels in WM. The over-amplified spurious peaks may lead to a higher chance of erroneous streamlines, if the “peak-heights” are used as part of the thresholding criteria in the fiber tracking step.

The spatially variant weights: For each voxel in the brain, the three-dimensional Euclidean distance to the WGB surface was calculated, and used to generate the relative weighting factor between the two datasets at that location. In general, closer to the cortex, the ODFs obtained from the 1.0 mm, b=1.5k dataset were more heavily weighted, and further into WM, the ODFs obtained from the 2.0 mm, b=8k dataset were more heavily weighted.

Rationale for this weighting scheme is provided below. First of all, inside the cerebral cortex, we set the weighting on the 1.0 mm, b=1.5k dataset to 1, to maximally preserve the spatial resolution in the 1.0 mm, b=1.5k dataset. In deep white matter, we found the 2.0 mm, b=8k dataset alone yields ODFs of the best angular resolution for crossing structures (see Figure 7), presumably because averaging with the 1.0 mm, b=1.5k dataset deteriorates the apparent angular resolution. Thus, it is helpful to set a large weight on the 2.0 mm, b=8k dataset to preserve the high angular resolution. Lastly, we choose the exponential function due to its mathematical convenience of gradually decreasing to zero, because a smooth transition between cortical GM (fully weighted by the 1.0 mm b=1.5k dataset) and deep WM (strongly weighted by the 2.0 mm b=8k dataset) might be helpful, especially for tractography. In the subjacent WM, we use the linear function to promote slightly higher

weighting on the high resolution dataset because we expect fewer crossing fibers here. Therefore, the final weighting, w , is the composite of these two functions, which is written as a function of the distance (d) from the center of the voxel to the WGB surface (Figure 1),

$$w = \begin{cases} 1, & d \leq 0 \\ 1 - \frac{d}{d_1}, & 0 < d \leq \hat{d} \\ e^{-\frac{d}{d_2}}, & d > \hat{d} \end{cases}$$

where \hat{d} represents the range of subjacent WM, which is related to d_1 and d_2 by

$$1 - \frac{\hat{d}}{d_1} = e^{-\frac{\hat{d}}{d_2}}, \quad d_1 \text{ determines the slope of the transition between GM and deep WM, and } d_2 \text{ is mainly used to control the weighting factor far away from the cerebral cortex.}$$

The weighting on the 2.0 mm, $b=8k$ dataset is then defined as $1-w$, and the combined ODF was calculated as the weighted summation of the ODFs calculated separately from the two datasets. The ODFs generated with the distance-based weighting (referred to as “Distance-W”) was later compared with the individual datasets and to the ODFs generated with equally weighting between the two (referred to as “Half-Half”).

Contrast to noise ratio estimates—A Jackknife resampling (“delete-d-observations”) analysis was performed to assess the reliability of the resulting ODFs from the 2.0 mm, $b=8k$ dataset, the 1.0 mm, $b=1.5k$ dataset, and the HIBRID datasets (Half-Half and Distance-W), respectively. Each time 20% of directions were randomly drawn and left out, and thus each Jackknife sample was comprised of 80% of total DW directions. A total number of 200 Jackknife samples were drawn. According to Shao and Tu (Shao and Tu, 1995), the variance across the 200 evaluations of ODF, $\text{Var}_{\text{SJACK-d}}^2$, was calculated as

$$\text{Var}_{\text{SJACK-d}} = \frac{r}{d} \cdot \left[\frac{1}{m} \sum_{t=1}^m \left(\mathbf{T}_{r, s_t} - \frac{1}{m} \sum_{k=1}^m \mathbf{T}_{r, s_k} \right)^2 \right] \quad [1]$$

where r is the number of data points included, d is the number of data points left out, m is the number of Jackknife samples drawn, and \mathbf{T}_{r, s_t} is the ODF evaluated with the t^{th} sample S_t .

The Contrast-to-Noise Ratio (CNR) was defined as the ODF amplitude over the square root of variance, averaged across all sampling directions. Specifically,

²By “SJACK-d” we refer to a sub-collection of Jackknife samples. A complete delete-d-Jackknife-resampling requires $N=C(n, d)$ evaluations, where n is the total number of DW directions, and d is the number of directions to be left out, i.e., $n=r+d$. The computational burden of a complete resampling is extensive. For example, consider a dataset of 120 DW directions. If 24 directions are left out, there are $C(120, 24) \approx 10^{25}$ unique subsets. So a sub-collection of Jackknife samples was used to approximate the variance of the ODF estimates, $\text{Var}_{\text{SJACK-d}}$. According to previous analyses (Shao and Tu, 1995), the number of samples drawn, m , needs to be greater than n to get an efficient approximation of $\text{Var}_{\text{SJACK-d}}$. In our case, $m = 200$, $n = 60$ or 120 . For more details, see “random subsampling of the delete-d Jackknife” in Shao and Tu (1995).

$$\text{CNR} \triangleq \frac{1}{N_{\text{dir}}} \sum_{i=1}^{N_{\text{dir}}} \frac{I_i}{\sqrt{\text{Var}_{\text{SJACK-d}, i}}} \quad [2]$$

$$I_i = \overline{T_{r,1}} - \min_i(\overline{T_{r,1}})$$

$$\overline{T_r} = \frac{1}{m} \sum_{k=1}^m T_{r, s_k}$$

where $\overline{T_r}$ is the mean ODF across 200 Jack-knife samples, I_i is the ODF amplitude above baseline in the i^{th} sampling direction, and N_{dir} is the total number of ODF sampling directions.

Fiber tracking—The fiber tracts and the Tract Density Imaging (TDI) maps (Calamante et al., 2010) were calculated using the deterministic streamline fiber tracking tool in DSI Studio (Yeh et al., 2013). The threshold of peak amplitude was automatically calculated for each dataset by default (Otsu, 1979). Other fiber tracking parameters include: a maximum turning angle of 60° , a step size of 0.5 mm, a minimum and maximum length threshold of 30 mm and 200 mm respectively. A spherical region of interest (ROI) was manually drawn in the centrum semiovale, and 10,000 streamlines passing through the ROI were selected to appreciate the difference in the trajectories of the tracts. For TDI maps, 2 million streamlines were generated for each dataset, and the maps were obtained using the TDI calculation tool in DSI Studio. The TDI maps were calculated on 0.25 mm isotropic grids.

3. Results

3.1. Distortion correction and registration

A $b \approx 0$ image is shown before and after the susceptibility distortion corrections for both 1.0mm and 2.0mm acquisitions (Figure 2). Different phase encoding directions yield different EPI-based distortions and neither of the images lines up well with pial surface (yellow contour) calculated from the T1w MEMPRAGE image. After the TOPUP correction, the pial surface is well aligned with EPI images. Results also indicate the 6 DOF boundary based registration is sufficient for the registration between T1w image and the corrected $b \approx 0$ image. The influence of the local susceptibility-induced signal dropout and residual distortions in the most challenging brain region (inferior temporal) is minimal to the global registration (Supplementary Material, Figure S6.a). A GIF file was included in the Supplementary Material (GIF_registration_2mm_to_1mm.gif) that automatically flips through the 1.0 mm $b \approx 0$ image and 2.0 mm $b \approx 0$ image before and after the motion correction.

3.1. Impact of Spatial Resolution on Resolving Cortical Structures

Figure 3 shows the PDDs calculated from the 1.0 mm, $b=1.5k$ dataset and the 2.0 mm, $b=8k$ dataset. Differences are mainly found in cortical sulcal walls, where the PDDs radial to the cortical surface are better revealed in the 1.0 mm, $b=1.5k$ dataset. The partial volume effect

with adjacent WM fiber bundles, leading to a reduction in radially within the GM, is more prominent in the 2.0 mm, b=8k dataset.

The PDDs are sampled from 20% of cortical thickness inside WM to 60% of cortical thickness into GM to appreciate the transition of the PDD from being tangential to radial with respect to each surface. As illustrated in Figure 4, this transition was found to be slower in the low-resolution data than in the high-resolution data. For example, the 2.0 mm, b=8k dataset shows primarily tangential PDDs in deep GM (e.g., as shown by the red line-segments representing the PDDs at 20% cortical thickness into GM in Figure 4a). In comparison, the 1.0 mm, b=1.5k dataset (Figure 4b) shows greater angles between the PDDs and the surface at the same depth, which are comparable to the PDDs seen at the depth of 40% or 60% cortical thickness into GM (as shown by the blue and yellow line-segments in Figure 4a) in the 2.0 mm, b=8k dataset by visual inspection. A similar phenomenon is also observed on the whole-brain radially map below (Figure 5–6), which is presumably responsible for the “belated turns” with respect to cortical depth in fiber tracking.

The radially results of four subjects are shown in Figure 5. In the 1.0 mm, b=1.5k dataset, the radially values on the pial surface were found to be lower than the intermediate surfaces (i.e., 20–80% of cortical thickness). At middle depths, such as 40% and 60% of cortical thickness, both datasets reveal a stripe of lower radially in the somatosensory cortex. These results are in close agreement with previous findings (McNab et al., 2013b). In addition, the radially values on the intermediate surfaces between WGB and pial (not including the WGB or pial surface) were found to be universally higher in the 1.0 mm, b=1.5k dataset than the 2.0 mm, b=8k dataset. Specifically, increased radially on the deeper surfaces (for example, 20% of cortical thickness) was consistently seen in all subjects over the entire brain, which will improve the capability in capturing the sharp turning features of the peri-cortical axonal fibers. Right hemisphere shows identical results (Supplementary Material, Figure S4).

Figure 6 shows radially histograms at different spatial resolutions (2.0 mm, 1.5 mm, and 1.0 mm) and different locations relative to cortical folds at matched b value (1500 s/mm²). In gyral crowns, the histograms of different spatial resolutions overlap with each other throughout cortical depths, except for the pial surface (the gyral crown is defined by a range of curvature value, and thus a range of radially values were seen on deeper surfaces). In gyral walls and fundi, different spatial resolutions were found to differ for the intermediate depths. In general, as the spatial resolution increases, the measured radially values increase, likely due to reduced partial volume with WM. The difference between different resolutions is most remarkable on surfaces that are relatively deep in the cortex, e.g., the surfaces of 20% and 40% of cortical thickness into GM (also see Figure S7 in Supplementary Material). This observation agrees with a previously described model (Van Essen et al., 2014) whereby the fibers go into the cortex without bending at the crowns, but have to bend to enter the sulcal walls and fundi, and adds to the supportive experimental evidence reported in previous studies (McNab et al., 2013b; Reveley et al., 2015; Sotiropoulos et al., 2016). In brief, by increasing the spatial resolution from 2.0 mm to 1.0 mm, we are better able to resolve the radial diffusion pattern immediately across the WGB in the deep cortex, which better reflects the known microanatomical features of the cerebral cortex.

3.2. HARDI Characteristics

The q-ball reconstruction of the 1.0 mm, $b=1.5k$ and the 2.0 mm, $b=8k$ datasets are visually inspected (Figure 7). The crossing structures in WM regions are better revealed with the 2.0 mm, $b=8k$ dataset (Figure 7a–b). Within cortex, the primary ODF peaks of the 2.0 mm, $b=8k$ dataset are largely tangential to the cortical ribbon (Figure 7c), likely reflecting the partial volume contamination of tangentially oriented WM just beneath the WGB. The primary ODF peaks in the 1.0 mm, $b=1.5k$ dataset are more radial (Figure 7d). This finding was consistent with the DTI results (Figure 3). The radial components emerged in the secondary peaks at middle to superficial depths of the cortex in the 2.0 mm, $b=8k$ dataset, but the tangential fiber directions are still present, again, likely a reflection of the partial volume effects between WM and GM (Figure 7c). The radial fiber direction was not clearly seen at the WGB, indicating the signal was strongly dominated by underlying WM at this depth. Similar results were found when $L_{\max} = 8$ and $\lambda = 0.006$ was used for both datasets (Supplementary Material, Figure S2), suggesting the observed differences in ODFs are not driven by the difference in ODF analysis parameters.

3.3. Reliability and Sensitivity Assessment using Jackknife Resampling

The results from the Jackknife analysis are shown in Figure 8. The average ODFs of the 200 Jackknife samples is displayed in opaque color, and errors (3 times standard deviations, SDs) are shown in transparent gray. The low SDs of the 2.0 mm, $b=8k$ dataset indicates high reliability in WM, but in superficial cortical GM the reliability dropped dramatically and spurious peaks are commonly seen in the average ODFs. The 1.0 mm, $b=1.5k$ dataset shows better reliability in cortical GM as well as in WM voxels with only a single fiber compartment, but in centrum semiovale voxels with crossing fibers peaks with small crossing angles merge into one amorphous blob, reflecting a deficiency in resolving crossing structures. The deficiency of the 1.0 mm, $b=1.5k$ data is also reflected in the larger SDs estimates compared to the 2.0 mm, $b=8k$ dataset. The performance of the Half-Half HIBRID dataset is somewhere in between judging by the angular resolution in WM crossing region, the spatial resolution in cortical GM, as well as the overall reliability. The Distance-W HIBRID dataset demonstrates reasonable reliability and preserves both of the angular and spatial resolution advantages in individual datasets.

The CNR maps derived from Jackknife resampling are shown in Figure 9. Overall, the 2.0 mm, $b=8k$ dataset shows the best CNR. The Half-Half HIBRID data showed better CNR than the 1.0 mm, $b=1.5k$ data in WM, which was mainly benefited by the 2.0 mm, $b=8k$ dataset. The Half-Half weighting somewhat deteriorates the CNR in WM, as compared to the 2.0 mm, $b=8k$ dataset alone. The HIBRID data using the Distance-W method largely retained the CNR in the 2.0 mm, $b=8k$ dataset. We also noticed some inhomogeneity in the CNR map, because the top of the head (vertex) has a greater number of Rx elements contributing and thus the high SNR pattern extends a bit deeper than at the temporal lobes. Also, we move the subjects head up until it touches, but there is some space in the LR direction, which would place their temporal lobes farther from the coil elements.

3.4. Tractography-based Assessments

Figure 10 shows the trajectory streamlines passing through a spherical ROI (diameter = 11 mm) manually drawn in the centrum semiovale. Figure 10 also shows a zoomed region where the streamlines enter cortical GM. For the 2.0 mm, b=8k dataset the streamlines proceed straight towards the gyral crowns and do not bend into gyral walls. The HIBRID datasets (Half-Half and Distance-W) both show streamlines curving into cortex from the WM near the gyral walls, as expected based on the known microanatomy. The Distance-W method shows slightly sharper turns. The 1.0 mm, b=1.5k dataset also shows streamlines curving into the cortex along gyral walls, but does not show the fibers penetrating the crossing region in deep WM (see arrows in Figure. 10) compared to the higher b-value datasets. This is presumably a result of the reduced angular resolution seen in Figure 8. In contrast, both of the HIBRID datasets (Half-Half and Distance-W) show contralateral connections through this crossing region, while the Distance-W HIBRID data reveals slightly more tracts in the superior longitudinal/arcuate fasciculus. Overall, the fiber tracking trajectories obtained using the Distance-W HIBRID data appear to best represent the known WM anatomy.

The TDI maps are shown in Figure 11. The 1.0 mm, b=1.5k dataset fail to recover streamlines in deep WM regions with multiple crossing fiber bundles (Figure 11b). Thus, the streamlines obtained are shorter in length and the overall “tract density” is lower (Figure 11a), since the total number of streamlines is fixed in the analysis. The major WM tracts are largely consistent between the 2.0 mm, b=8k and the HIBRID datasets (Figure 11a), while more streamlines were found in the 2.0 mm, b=8k dataset and the Distance-W HIBRID dataset than the Half-Half HIBRID dataset (Figure 11b). Between the 2.0 mm, b=8k dataset and the Distance-W HIBRID dataset (Figure 11c), the latter reveals more streamlines extending across the WGB into the cortical GM. A group TDI maps averaged across all four subjects was provided in Supplementary Materials (Figure S5)

4. Discussion

In this study, we demonstrate a framework to acquire and integrate the complementary benefits of high b-value diffusion imaging data and high spatial resolution imaging data. We use the distance from the WGB surface to determine the weighting between a high b-value but low spatial resolution dataset and a high spatial resolution but low b-value dataset, to provide a smooth transition between the two datasets and to allow a combination that depends on the imaging capability most needed to resolve local structures. The quality of the resulting HIBRID data was assessed using ODF metrics, which demonstrates reasonable reliability and CNR in both cortical GM and deep WM regions.

Several recent methods have been described which attempted to achieve a similar goal to the HIBRID method. The RubiX method (Sotiropoulos et al., 2016) was extended from its single shell model (Sotiropoulos et al., 2013) to allow the fusion of 1.05 mm 7T data ($b = 1000b = 2000 \text{ s/mm}^2$) with 1.25 mm with high angular resolution 3T data ($b = 1000b = 2000, 3000 \text{ s/mm}^2$). The extended RubiX allows more flexibility in data acquisition and reported improved tractography in both cerebral WM and cortex. Alexander et al. (Alexander et al., 2015) demonstrated that a number of desired features (such as high spatial

resolution and multi-shell diffusion contrasts) can be learned from high quality data using a machine learning approach and then transferred to a shorter MRI scan that is independent from the training data.

In comparison, our approach samples a larger range of k- and q-space, each of which pushes to the limit of either k- or q-space sampling by compromising the other. The cortical ribbon and the distance from the white-gray boundary was used as a natural coordinate system to provide approximate guidance of what imaging capability is most needed to resolve local structures. We aim to resolve local structures with the best informative data, and the distance-based weighted function gives a very clear description of how much of the information comes from each dataset. We used half of the high k- and half of the high q-datasets to generate the HIBRID data so that the total acquisition time is approximately matched with the high k- and high q-datasets standing alone. The q-ball ODF was used to illustrate the framework, because it is a “model-free” approach to reveal the diffusion contrasts inherent to the acquired data, which would be an intuitive way to motivate the method. The RubiX method (Sotiropoulos et al., 2016; Sotiropoulos et al., 2013) uses generative models of the data to fuse datasets, while the data fusion approach presented in the current study combines ODFs directly. Both data fusion strategies have potential advantages and disadvantages that would be important to investigate in a subsequent study. The smoothly decaying relative weighting from the WGB surface used in the current study is a pragmatic simplification of the neural anatomy, but seems to be effective in facilitating improvements in fiber orientation estimates without requiring dedicated data mining procedures. However, machine learning approaches and other more sophisticated modeling and/or analysis approaches can be adapted into the HIBRID framework, including the RubiX and the quality transfer methods mentioned above.

To assess the performance of alignment between the 1.0 mm, b=1.5k dataset and the 2.0 mm, b=8k dataset, we: qualitatively check the anatomical features using grayscale images (i.e., $b \approx 0$ image and FA maps) to confirm that the two datasets overlap well; and quantitatively examine the directional consistency inside WM regions (Supplementary Material, Figure S1), which shows good alignment between the two datasets. To minimize anatomical misalignments, we made every effort to control the geometric distortions including fixing the echo spacing and FOV along the PE direction. Yet, it is suboptimal from the SNR perspective to match the echo spacing. On a conventional scanner when SNR becomes more deprived in the high b-value acquisition, it would be more practical to minimize the echo spacing to shorten TE. The concern on geometric misalignment is minimal if the distortions are properly corrected in the preprocessing step (see Appendix A in (Sotiropoulos et al., 2016)). The optimization of HIBRID on conventional scanner is beyond the scope of this study, but we acquired an additional dataset with $G_{\max} = 80\text{mT/m}$ (equivalent to Prisma) to demonstrate the feasibility of HIBRID on more widely available research scanners (Supplementary Material, Figure S3).

Several ODF and tractography metrics were shown to exemplify the complementary advantages in the fused HIBRID data. A simultaneous improvement in both WM and cortical GM tractography will be beneficial in improving the spatial specificity of connectivity measurement in neurobiological research (Nummenmaa et al., 2014). The the

advantages of the Distance-W method over the Half-Half weighted method are only marginal near the WGB (Figure 10), although the Distance-W dataset has a better reliability and spatial resolution in cortical GM (Figure 8) and higher CNR in WM (Figure 9) on the ODF level. This is likely because fiber tracking algorithms assume smoothness between consecutive steps, and the fiber direction is determined from an interpolated neighborhood. As a result, the high spatial resolution information at tissue boundaries (e.g., the WGB) is smoothed out. Intelligent strategies to handle the 90° turns properly are required before more striking benefits can be gained, and recent work (Cottaar et al., 2016) has shed a light towards this goal. The inhomogeneous SNR leads to some inhomogeneity in the ODF-based CNR map (Figure 9). For tractography, it likely places importance on smarter, data-driven (CNR driven) threshold choices. The tractography results were assessed by visual inspection in this study, partly due to lack of gold-standard information. It will be helpful to find out a quantitative measure of tractography performance in the future.

The current work can be further improved. First of all, the weighting function for data integration is based on the distance from the WGB, which is based on a simplified model of brain anatomy. Weighting one of the datasets to zero essentially eliminates some of the data. As bad as that sounds, it may well be the right thing to do. Close to the WGB, the partial volume effects and signal loss at high b value are substantial barriers to studying intra-cortical structures. To resolve the detailed cortical laminar and columnar structures within cortex, a more dedicated imaging protocol might be needed, which is beyond the goal of the current work. In our study, the 2.0mm, b=8k datasets reveals only tangential diffusion in deep GM (Figure 8). In this scenario, incorporating the high b- data barely adds any benefits but introduces partial volume artifacts. In deep white matter, the angular resolution and reliability of the 1.0mm, b=1.5k dataset are much lower than the 2.0mm, b=8k dataset (Figure 8), and thus the relative weighting on the 1.0mm, b=1.5k was also set to be much lower. Nevertheless, it would be helpful to investigate an explicit data-driven weighting strategy. For example, the length scale of local structures can be inferred by examining the coherence (e.g., of ODFs) among neighboring voxels and between two datasets, which can be used to refine the weighting accordingly. The current weighting function neglects the preferences of subcortical structures. For studies with a focus on subcortical-cortical connectivity, modifications of the imaging parameters or pulse sequence should be considered to increase the SNR in the region, and the weighting function should be adjusted accordingly.

Second, the EPI distortion correction step involves image interpolation and un-warping, which effectively decreases the intrinsic spatial resolution. This distortion correction is mainly needed to bring the cortical surfaces generated from a minimally distorted T1w MEMPRAGE image into geometric correspondence with the EPI-based diffusion data. We can alternatively generate the required surfaces from a T1w image data using the same EPI readout and thus generating the same image distortions as the diffusion data (Renvall et al., 2016) to avoid the interpolation and image warping step. Newly developed super high resolution diffusion MRI techniques (Chang et al., 2015; Guhaniyogi et al., 2016; Haldar et al., 2016; Setsompop et al., 2017), also look promising for improving high spatial resolution diffusion, especially of the cerebral cortex.

Also, the preprocessing pipeline is suboptimal. Ideally, TOPUP would be run on the two datasets, saving but not applying the distortion fields. Then the field map together with motion estimates would be input to EDDY and all the warping (eddy current + susceptibility distortions) would be corrected in one step (<http://fsl.fmrib.ox.ac.uk/fsl/fslwiki/eddy/UsersGuide>). In the current study, the two datasets are of different spatial resolutions by design, and thus TOPUP was performed and applied separately for each, before the two datasets were concatenated for a joint eddy current correction, which introduced extra steps of interpolation. Future improvement will incorporate a composite warp field that integrates all spatial transformations and nonlinear warps, which can be applied to the initial unprocessed images directly. To elucidate the potential confounds from preprocessing procedures, in the spatial resolution comparison with the fixed b-value of 1500 s/mm² (Figure 6), the pre-processing was performed in their native resolutions, the TOPUP results were input to EDDY and both corrections were applied in one step. Results evidenced that the differences seen between spatial resolutions are intrinsic to the data rather than driven by preprocessing procedures.

In general, it will always be beneficial to improve the sensitivity of the diffusion acquisition to allow increases in spatial resolution or diffusion angular resolution, or both. Methods that might allow this include fundamental improvements in coil (Keil et al., 2013; Wiggins et al., 2006) as well as high field technology (Heidemann et al., 2012), or sequence innovations such as Simultaneous MultiSlice (Larkman et al., 2001) with blipped-CAPI (Setsompop et al., 2012a; Setsompop et al., 2012b). Improvements in overall sensitivity of high b-value scans come with improved gradient technology (McNab et al., 2013a; Setsompop et al., 2013).

In practice, these experimental feasibilities altogether will determine the specific acquisition limits. The goal of HIBRID is a spatially varying tradeoff which allows local regions to be more heavily weighted by the most informative dataset, and thus each dataset will represent roughly the practical acquisition limits for either spatial resolution or b-value accordingly. For different acquisitions, it will be beneficial to adjust the analysis methods accordingly as well. For example, the spherical deconvolution method (Anderson, 2005; Dell'Acqua et al., 2007; Tournier et al., 2004) is known to be able to resolve crossing structures at lower b-value compared to QBI, if the deconvolution kernel can be properly estimated for different tissues (see Jeurissen et al. (Jeurissen et al., 2014) for example). Similar model-based HARDI methods can hence potentially enhance the feasibility of extending the HIBRID method into clinical practice. In patient populations, cortical lesions may yield poor the grey-white contrasts and cause errors in the surface reconstructions needed for our method. These errors usually can be semi-manually corrected during the FreeSurfer pipeline and thus will not preclude the feasibility of the HIBRID method in patient populations.

5. Conclusions

The HIBRID method is motivated by the tradeoff between k and q resolution forced by the finite availability of SNR in diffusion MRI experiments. The brain is composed of different anatomical structures by nature, some of those features are best captured by high-k acquisitions, and others more high-q acquisitions. Here we demonstrated the advantages of

acquiring two datasets, each of which roughly represents the practical acquisition limits of the high-k and high-q capabilities, so that a spatially varying tradeoff can be used to allow local regions to be more heavily weighted by the most informative dataset. Results show remarkable improvements in ODF and tractography metrics without intensive datamining procedures. We discussed the flexibility of incorporating improvements and/or adjustments in the HIBRID framework, which may improve its significance and feasibility in neurobiological studies of the brain.

Supplementary Material

Refer to Web version on PubMed Central for supplementary material.

Acknowledgments

The authors thank Drs. Kathleen S. Rockland and Karl Zilles for helpful discussions on connective neuroanatomy in the brain. We thank Drs. Caroline Magnain and Bruce Fischl for providing OCT images of human brain samples. Acknowledgements also go to Dr. Fang-Cheng F. Yeh for providing help with DSI-Studio tools, and Dr. Ruopeng Wang for assistance with FreeView visualization tools. The work is supported by funding from the National Institutes of Health Blueprint Initiative for Neuroscience Research Grant U01-MH093765, NIBIB grant P41-EB015896 and the Instrumentation Grants S10-RR023401, S10-RR023043, and S10-RR019307. Funding support was also received from the MGH Executive Committee on Research Fund for Medical Discovery Fellowship Award.

References

- Aganj I, Lenglet C, Sapiro G, Yacoub E, Ugurbil K, Harel N. Reconstruction of the orientation distribution function in single- and multiple-shell q-ball imaging within constant solid angle. *Magn Reson Med*. 2010; 64:554–566. [PubMed: 20535807]
- Alexander DC, Zikic D, Wotschel V, Zhang J, Zhang H, Criminisi A. Image quality transfer: exploiting bespoke high-quality data to enhance everyday acquisitions. *Proc ISMRM*. 2015:0563.
- Anderson AW. Measurement of fiber orientation distributions using high angular resolution diffusion imaging. *Magn Reson Med*. 2005; 54:1194–1206. [PubMed: 16161109]
- Andersson JL, Skare S, Ashburner J. How to correct susceptibility distortions in spin-echo echo-planar images: application to diffusion tensor imaging. *Neuroimage*. 2003; 20:870–888. [PubMed: 14568458]
- Andersson JL, Sotiropoulos SN. An integrated approach to correction for off-resonance effects and subject movement in diffusion MR imaging. *Neuroimage*. 2016; 125:1063–1078. [PubMed: 26481672]
- Calamante F, Tournier JD, Jackson GD, Connelly A. Track-density imaging (TDI): super-resolution white matter imaging using whole-brain track-density mapping. *Neuroimage*. 2010; 53:1233–1243. [PubMed: 20643215]
- Chang HC, Sundman M, Petit L, Guhaniyogi S, Chu ML, Petty C, Song AW, Chen NK. Human brain diffusion tensor imaging at submillimeter isotropic resolution on a 3Tesla clinical MRI scanner. *Neuroimage*. 2015; 118:667–675. [PubMed: 26072250]
- Cottaar M, Bastiani M, Chen C, Dikranian K, Van Essen DC, Behrens TE, Sotiropoulos SN, Jbabdi S. Fibers crossing the white/gray matter boundary: a semi-global, histology-informed dMRI model. *Proc ISMRM*. 2016:0123.
- Dale AM, Fischl B, Sereno MI. Cortical surface-based analysis. I. Segmentation and surface reconstruction. *Neuroimage*. 1999; 9:179–194. [PubMed: 9931268]
- Dell'Acqua F, Rizzo G, Scifo P, Clarke RA, Scotti G, Fazio F. A model-based deconvolution approach to solve fiber crossing in diffusion-weighted MR imaging. *IEEE Trans Biomed Eng*. 2007; 54:462–472. [PubMed: 17355058]

- Descoteaux M, Angelino E, Fitzgibbons S, Deriche R. Regularized, fast, and robust analytical Q-ball imaging. *Magn Reson Med*. 2007; 58:497–510. [PubMed: 17763358]
- Fan Q, Nummenmaa A, Witzel T, Zanzonico R, Keil B, Cauley S, Polimeni JR, Tisdall D, Van Dijk KR, Buckner RL, Wedeen VJ, Rosen BR, Wald LL. Investigating the capability to resolve complex white matter structures with high b-value diffusion magnetic resonance imaging on the MGH-USC Connectom scanner. *Brain Connect*. 2014; 4:718–726. [PubMed: 25287963]
- Fan Q, Witzel T, Nummenmaa A, Van Dijk KR, Van Horn JD, Drews MK, Somerville LH, Sheridan MA, Santillana RM, Snyder J, Hedden T, Shaw EE, Hollinshead MO, Renvall V, Zanzonico R, Keil B, Cauley S, Polimeni JR, Tisdall D, Buckner RL, Wedeen VJ, Wald LL, Toga AW, Rosen BR. MGH-USC Human Connectome Project datasets with ultra-high b-value diffusion MRI. *Neuroimage*. 2016; 124:1108–1114. [PubMed: 26364861]
- Feinberg DA, Moeller S, Smith SM, Auerbach E, Ramanna S, Gunther M, Glasser MF, Miller KL, Ugurbil K, Yacoub E. Multiplexed echo planar imaging for sub-second whole brain fMRI and fast diffusion imaging. *PLoS ONE*. 2010; 5:e15710. [PubMed: 21187930]
- Feinberg DA, Setsompop K. Ultra-fast MRI of the human brain with simultaneous multi-slice imaging. *J Magn Reson*. 2013
- Fischl B. FreeSurfer. *Neuroimage*. 2012; 62:774–781. [PubMed: 22248573]
- Fischl B, Sereno MI, Dale AM. Cortical surface-based analysis. II: Inflation, flattening, and a surface-based coordinate system. *Neuroimage*. 1999; 9:195–207. [PubMed: 9931269]
- Greve DN, Fischl B. Accurate and robust brain image alignment using boundary-based registration. *Neuroimage*. 2009; 48:63–72. [PubMed: 19573611]
- Guhaniyogi S, Chu ML, Chang HC, Song AW, Chen NK. Motion immune diffusion imaging using augmented MUSE for high-resolution multi-shot EPI. *Magn Reson Med*. 2016; 75:639–652. [PubMed: 25762216]
- Haldar, JP., Fan, Q., Setsompop, K. Proc ISMRM. Singapore: 2016. Whole-brain quantitative diffusion MRI at 660 μm resolution in 25 minutes using gSlider-SMS and SNR-enhancing joint reconstruction; p. 0102
- Heidemann RM, Anwander A, Feiweier T, Knosche TR, Turner R. k-space and q-space: combining ultra-high spatial and angular resolution in diffusion imaging using ZOOPPA at 7 T. *Neuroimage*. 2012; 60:967–978. [PubMed: 22245337]
- Jenkinson M, Beckmann CF, Behrens TE, Woolrich MW, Smith SM. FSL. *Neuroimage*. 2012; 62:782–790. [PubMed: 21979382]
- Jeurissen B, Leemans A, Tournier JD, Jones DK, Sijbers J. Investigating the prevalence of complex fiber configurations in white matter tissue with diffusion magnetic resonance imaging. *Hum Brain Mapp*. 2013; 34:2747–2766. [PubMed: 22611035]
- Jeurissen B, Tournier JD, Dhollander T, Connelly A, Sijbers J. Multi-tissue constrained spherical deconvolution for improved analysis of multi-shell diffusion MRI data. *Neuroimage*. 2014; 103:411–426. [PubMed: 25109526]
- Keil B, Blau JN, Biber S, Hoecht P, Tountcheva V, Setsompop K, Triantafyllou C, Wald LL. A 64-channel 3T array coil for accelerated brain MRI. *Magn Reson Med*. 2013; 70:248–258. [PubMed: 22851312]
- Kleinnijenhuis M, van Mourik T, Norris DG, Ruiter DJ, van Cappellen van Walsum AM, Barth M. Diffusion tensor characteristics of gyrencephaly using high resolution diffusion MRI in vivo at 7T. *Neuroimage*. 2015; 109:378–387. [PubMed: 25585019]
- Larkman DJ, Hajnal JV, Herlihy AH, Coutts GA, Young IR, Ehnholm G. Use of multicoil arrays for separation of signal from multiple slices simultaneously excited. *J Magn Reson Imaging*. 2001; 13:313–317. [PubMed: 11169840]
- Magnain, C., Augustinack, JC., Konukoglu, E., Wedeen, V., Boas, D., Fischl, B. Human Brain Mapping Using Optical Coherence Tomography Biomedical Optics 2014. Optical Society of America; Miami, Florida: 2014a. p. BT3A.62
- Magnain C, Augustinack JC, Reuter M, Wachinger C, Frosch MP, Ragan T, Akkin T, Wedeen VJ, Boas DA, Fischl B. Blockface histology with optical coherence tomography: a comparison with Nissl staining. *Neuroimage*. 2014b; 84:524–533. [PubMed: 24041872]

- Magnain, C., Yendiki, A., Boas, D., Fischl, B. Using Optical Coherence Tomography to Validate Diffusion MRI. Organization for Human Brain Mapping; Seattle, WA, USA: 2013.
- McNab JA, Edlow BL, Witzel T, Huang SY, Bhat H, Heberlein K, Feiweier T, Liu K, Keil B, Cohen-Adad J, Tisdall MD, Folkerth RD, Kinney HC, Wald LL. The Human Connectome Project and beyond: initial applications of 300 mT/m gradients. *Neuroimage*. 2013a; 80:234–245. [PubMed: 23711537]
- McNab JA, Jbabdi S, Deoni SC, Douaud G, Behrens TE, Miller KL. High resolution diffusion-weighted imaging in fixed human brain using diffusion-weighted steady state free precession. *Neuroimage*. 2009; 46:775–785. [PubMed: 19344686]
- McNab JA, Polimeni JR, Wang R, Augustinack JC, Fujimoto K, Stevens A, Triantafyllou C, Janssens T, Farivar R, Folkerth RD, Vanduffel W, Wald LL. Surface based analysis of diffusion orientation for identifying architectonic domains in the in vivo human cortex. *Neuroimage*. 2013b; 69:87–100. [PubMed: 23247190]
- Miller KL, Stagg CJ, Douaud G, Jbabdi S, Smith SM, Behrens TE, Jenkinson M, Chance SA, Esiri MM, Voets NL, Jenkinson N, Aziz TZ, Turner MR, Johansen-Berg H, McNab JA. Diffusion imaging of whole, post-mortem human brains on a clinical MRI scanner. *Neuroimage*. 2011; 57:167–181. [PubMed: 21473920]
- Nummenmaa A, McNab JA, Savadjiev P, Okada Y, Hamalainen MS, Wang R, Wald LL, Pascual-Leone A, Wedeen VJ, Raji T. Targeting of white matter tracts with transcranial magnetic stimulation. *Brain Stimul*. 2014; 7:80–84. [PubMed: 24220599]
- Otsu N. A Threshold Selection Method from Gray-Level Histograms. *IEEE Transactions on Systems, Man, and Cybernetics*. 1979; 9:62–66.
- Polimeni JR, Bhat H, Witzel T, Benner T, Feiweier T, Inati SJ, Renvall V, Heberlein K, Wald LL. Reducing sensitivity losses due to respiration and motion in accelerated echo planar imaging by reordering the autocalibration data acquisition. *Magn Reson Med*. 2015
- Polimeni JR, Fischl B, Greve DN, Wald LL. Laminar analysis of 7T BOLD using an imposed spatial activation pattern in human V1. *Neuroimage*. 2010; 52:1334–1346. [PubMed: 20460157]
- Renvall V, Witzel T, Wald LL, Polimeni JR. Automatic cortical surface reconstruction of high-resolution T echo planar imaging data. *Neuroimage*. 2016; 134:338–354. [PubMed: 27079529]
- Reveley C, Seth AK, Pierpaoli C, Silva AC, Yu D, Saunders RC, Leopold DA, Ye FQ. Superficial white matter fiber systems impede detection of long-range cortical connections in diffusion MR tractography. *Proc Natl Acad Sci U S A*. 2015; 112:E2820–2828. [PubMed: 25964365]
- Setsompop K, Cohen-Adad J, Gagoski BA, Raji T, Yendiki A, Keil B, Wedeen VJ, Wald LL. Improving diffusion MRI using simultaneous multi-slice echo planar imaging. *Neuroimage*. 2012a; 63:569–580. [PubMed: 22732564]
- Setsompop K, Fan Q, Stockmann JP, Bilgic B, Huang S, Cauley S, Nummenmaa A, Wang F, Rathi Y, Witzel T, Wald LL. High-resolution in vivo diffusion imaging of the human brain with Generalized SLIce Dithered Enhanced Resolution Simultaneous MultiSlice (gSlider-SMS). *MRM* Accepted. 2017
- Setsompop K, Gagoski BA, Polimeni JR, Witzel T, Wedeen VJ, Wald LL. Blipped-controlled aliasing in parallel imaging for simultaneous multislice echo planar imaging with reduced g-factor penalty. *Magn Reson Med*. 2012b; 67:1210–1224. [PubMed: 21858868]
- Setsompop K, Kimmlingen R, Eberlein E, Witzel T, Cohen-Adad J, McNab JA, Keil B, Tisdall MD, Hoecht P, Dietz P, Cauley SF, Tountcheva V, Matschl V, Lenz VH, Heberlein K, Potthast A, Thein H, Van Horn J, Toga A, Schmitt F, Lehne D, Rosen BR, Wedeen V, Wald LL. Pushing the limits of in vivo diffusion MRI for the Human Connectome Project. *Neuroimage*. 2013; 80:220–233. [PubMed: 23707579]
- Shao, J., Tu, D. The jackknife and bootstrap. Springer Verlag; New York, NY, USA: 1995.
- Smith SM, Jenkinson M, Woolrich MW, Beckmann CF, Behrens TE, Johansen-Berg H, Bannister PR, De Luca M, Drobnjak I, Flitney DE, Niazy RK, Saunders J, Vickers J, Zhang Y, De Stefano N, Brady JM, Matthews PM. Advances in functional and structural MR image analysis and implementation as FSL. *Neuroimage*. 2004; 23(Suppl 1):S208–219. [PubMed: 15501092]
- Song AW, Chang HC, Petty C, Guidon A, Chen NK. Improved delineation of short cortical association fibers and gray/white matter boundary using whole-brain three-dimensional diffusion tensor

- imaging at submillimeter spatial resolution. *Brain Connect.* 2014; 4:636–640. [PubMed: 25264168]
- Sotiropoulos SN, Hernandez-Fernandez M, Vu AT, Andersson JL, Moeller S, Yacoub E, Lenglet C, Ugurbil K, Behrens TE, Jbabdi S. Fusion in diffusion MRI for improved fibre orientation estimation: An application to the 3T and 7T data of the Human Connectome Project. *Neuroimage.* 2016; 134:396–409. [PubMed: 27071694]
- Sotiropoulos SN, Jbabdi S, Andersson JL, Woolrich MW, Ugurbil K, Behrens TE. RubiX: combining spatial resolutions for Bayesian inference of crossing fibers in diffusion MRI. *IEEE Trans Med Imaging.* 2013; 32:969–982. [PubMed: 23362247]
- Tournier JD, Calamante F, Gadian DG, Connelly A. Direct estimation of the fiber orientation density function from diffusion-weighted MRI data using spherical deconvolution. *Neuroimage.* 2004; 23:1176–1185. [PubMed: 15528117]
- Tristan-Vega A, Westin CF, Aja-Fernandez S. Estimation of fiber orientation probability density functions in high angular resolution diffusion imaging. *Neuroimage.* 2009; 47:638–650. [PubMed: 19393321]
- Tuch DS, Reese TG, Wiegell MR, Makris N, Belliveau JW, Wedeen VJ. High angular resolution diffusion imaging reveals intravoxel white matter fiber heterogeneity. *Magn Reson Med.* 2002; 48:577–582. [PubMed: 12353272]
- van der Kouwe AJ, Benner T, Salat DH, Fischl B. Brain morphometry with multiecho MPRAGE. *Neuroimage.* 2008; 40:559–569. [PubMed: 18242102]
- Van Essen, DC., Jbabdi, S., Sotiropoulos, SN., Chen, C., Dikranian, K., Coalson, T., Harwell, J., Behrens, TEJ., Glasser, MF. *Diffusion MRI. Second.* Academic Press; San Diego: 2014. Chapter 16 - Mapping Connections in Humans and Non-Human Primates: Aspirations and Challenges for Diffusion Imaging; p. 337-358.
- White NS, Dale AM. Optimal diffusion MRI acquisition for fiber orientation density estimation: an analytic approach. *Hum Brain Mapp.* 2009; 30:3696–3703. [PubMed: 19603409]
- Wiggins GC, Triantafyllou C, Potthast A, Reykowski A, Nittka M, Wald LL. 32-channel 3 Tesla receive-only phased-array head coil with soccer-ball element geometry. *Magn Reson Med.* 2006; 56:216–223. [PubMed: 16767762]
- Wu YC, Alexander AL. Hybrid diffusion imaging. *Neuroimage.* 2007; 36:617–629. [PubMed: 17481920]
- Yeh FC, Verstynen TD, Wang Y, Fernandez-Miranda JC, Tseng WY. Deterministic diffusion fiber tracking improved by quantitative anisotropy. *PLoS ONE.* 2013; 8:e80713. [PubMed: 24348913]
- Zilles, K., Palomero-Gallagher, N., Gräßel, D., Schlömer, P., Cremer, M., Woods, R., Amunts, K., Axer, M. Chapter 18 - High-Resolution Fiber and Fiber Tract Imaging Using Polarized Light Microscopy in the Human, Monkey, Rat, and Mouse Brain - Rockland, Kathleen S *Axons and Brain Architecture.* Academic Press; San Diego: 2016. p. 369-389.

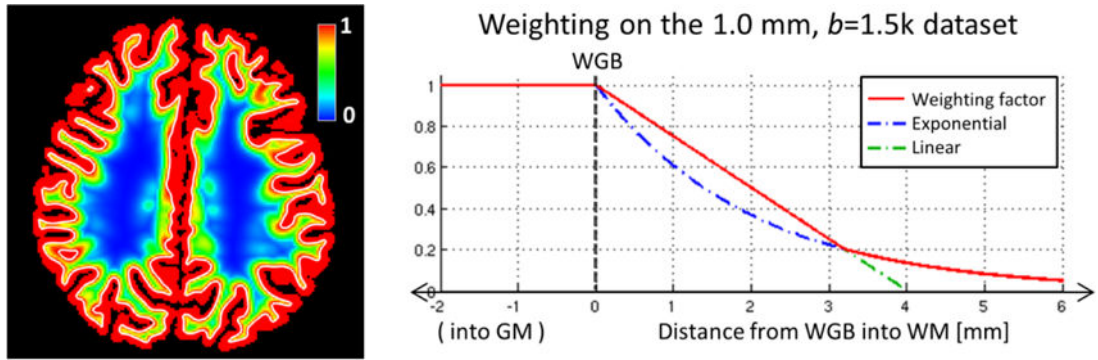


Figure 1.

The spatial weighting for the high resolution (1.0 mm, $b=1.5k$) dataset. Closer to the cortex, the high-resolution dataset is weighted more, while further away from the WGB, the high- b dataset is weighted more. In this case, $d_1 = 4$ mm, $d_2 = 2$ mm. The white contour in the left figure represents the WGB surface.

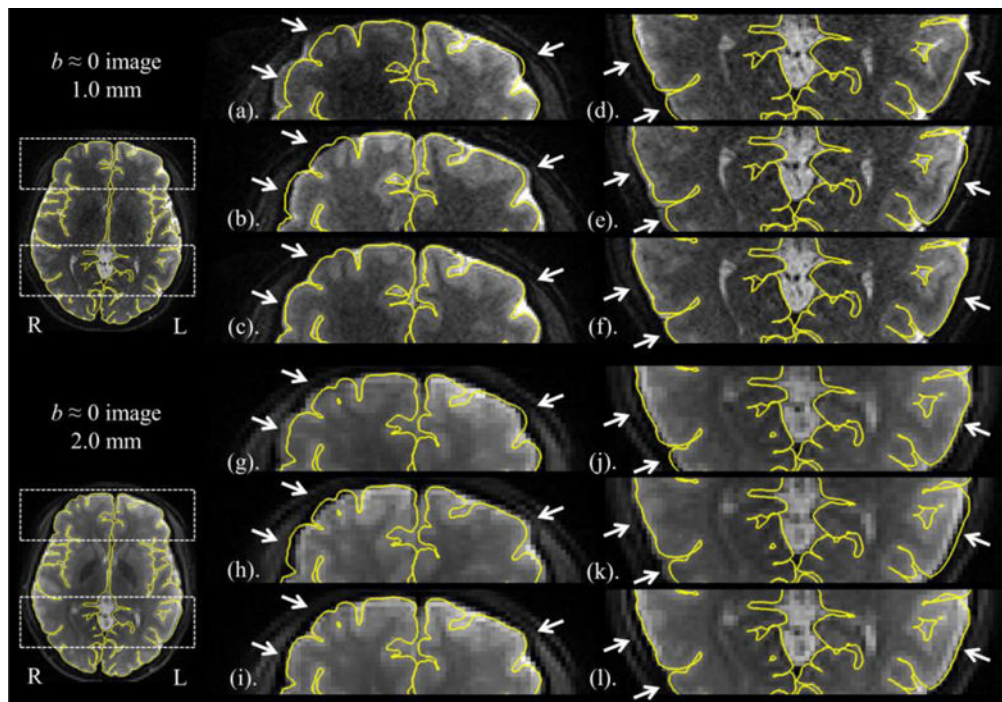


Figure 2.

$b \approx 0$ images before and after susceptibility distortion correction. A central axial slice of the $b \approx 0$ image is shown (a–f, 1.0 mm; g–l, 2.0 mm). The circled areas are zoomed in to appreciate the distortions with a PE direction of (a,d,g,j) $R \gg L$ or (b,e,h,k) $L \gg R$, compared to (c,f,i,l) the corrected image. The yellow and blue lines are the pial surface and the WGB respectively, which were calculated from the T1w MEMPRAGE image in FreeSurfer.

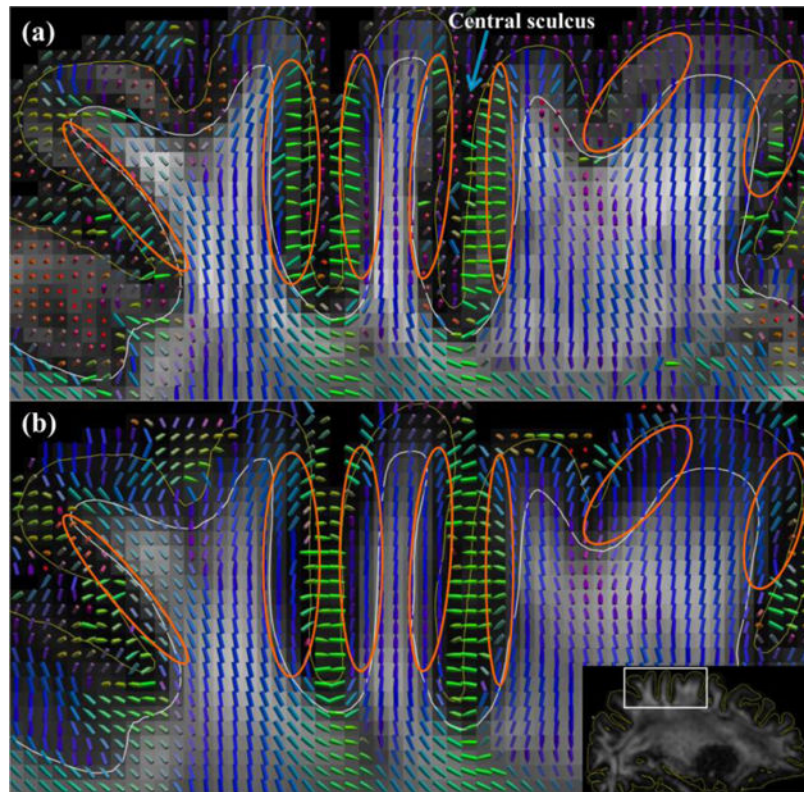


Figure 3. The primary diffusion directions calculated with the (a) 1.0 mm, b=1.5k dataset and the (b) 2.0 mm, b=8k dataset (up-sampled to 1.0mm voxel size after registration) are displayed on FA maps. The white contour represents the WGB surface and the yellow contour represents the pial surface.

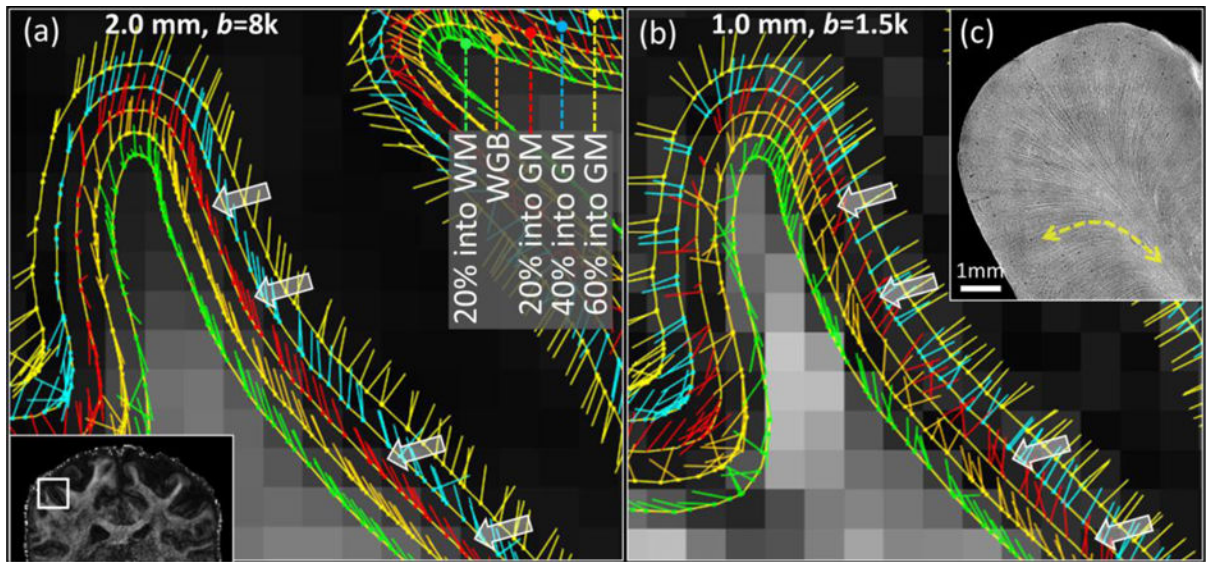


Figure 4.

The primary diffusion directions evaluated at various cortical depths. The surface at 20% cortical thickness into WM (green), the WGB surface (orange), and the surfaces at 20% (red), 40% (blue) and 60% (yellow) cortical thickness into GM are shown for (a) the 2.0 mm, $b=8k$ dataset and (b) the 1.0 mm, $b=1.5k$ dataset respectively. (c) An OCT image of an ex vivo sample of human temporal cortex is shown for an anatomical reference (Magnain et al., 2014a; Magnain et al., 2013).

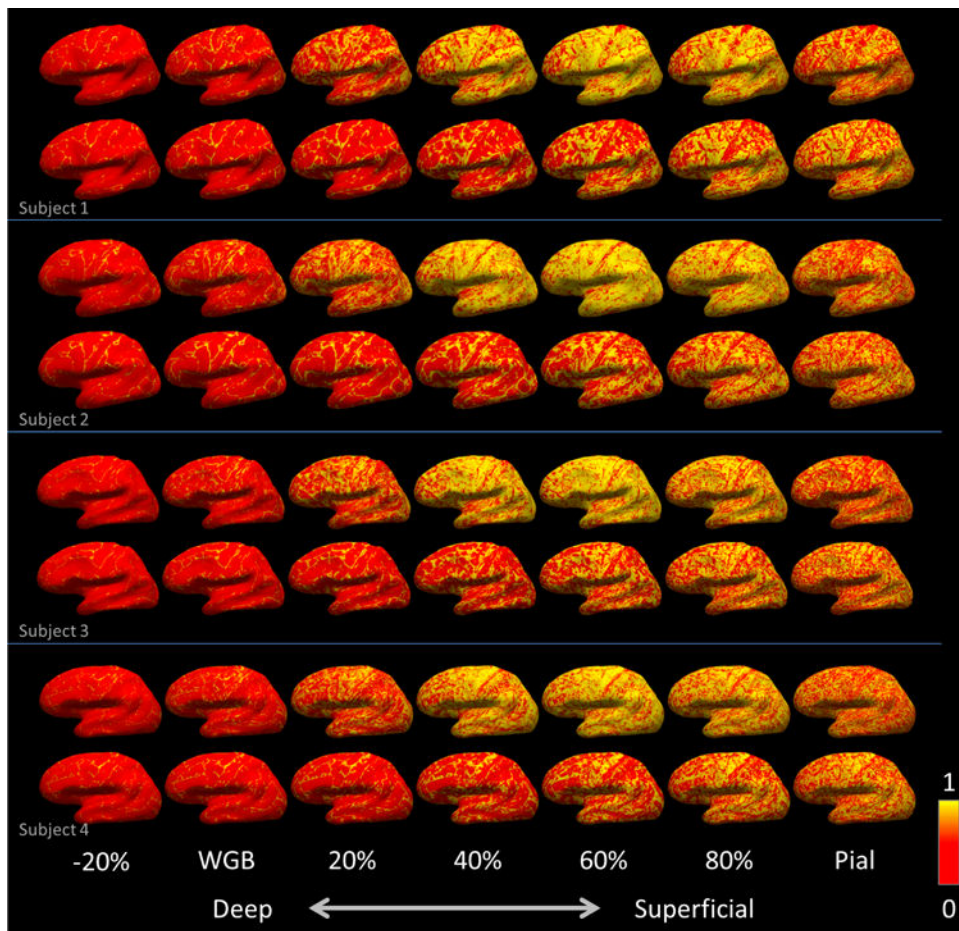


Figure 5.

The radiality map on the flattened brain surfaces in four subjects (left hemisphere). Every two rows correspond to one subject. The results from the 1.0 mm, $b=1.5k$ dataset are shown in the upper row, and the 2.0 mm, $b=8k$ dataset in the lower row. From left to right, the radiality indices are from deep to superficial depths. Specifically, they are evaluated at the surface of 20% cortical depth into WM (-20%), the WGB surface, the surfaces of 20%, 40%, 60% and 80% cortical thickness into GM, and the pial surface, respectively. The radiality values on the intermediate surfaces between the WGB and the pial surface are found to be universally higher in the 1.0 mm, $b=1.5k$ dataset than the 2.0 mm, $b=8k$ dataset.

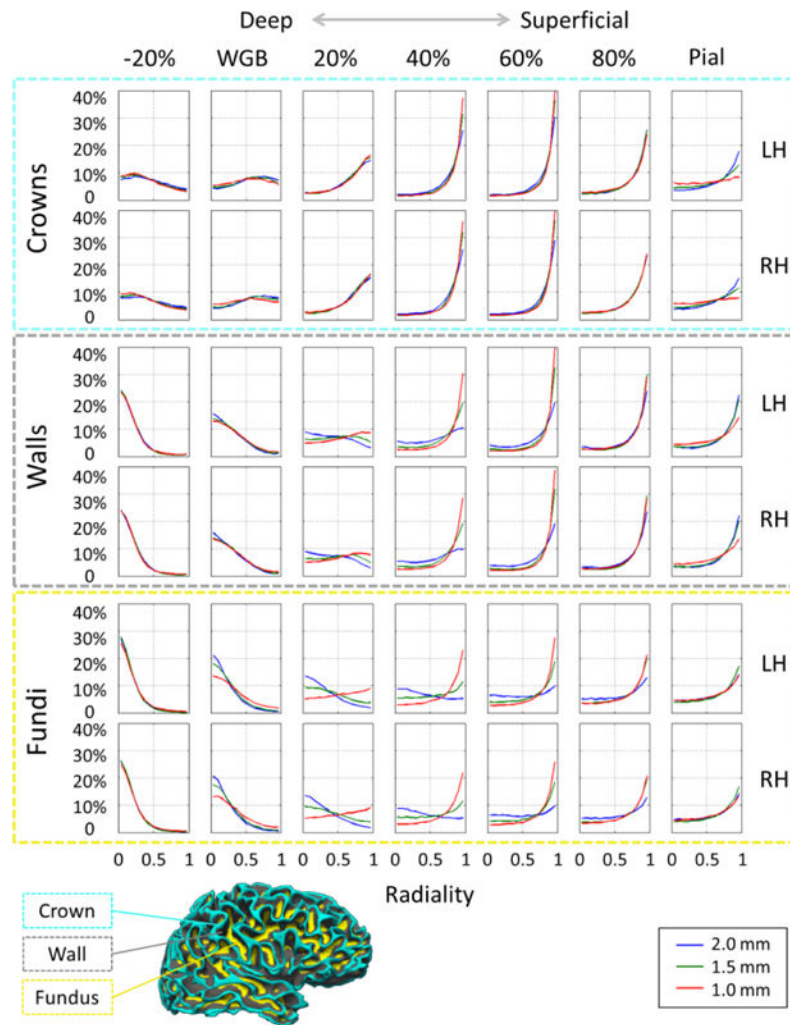


Figure 6.

The radiality histograms of gyral crowns, walls and fundi at various cortical depths. The most remarkable differences due to spatial resolutions were found in gyral walls and fundi deeper in the cortex, i.e., at 20% and 40% cortical depth, indicating that extra spatial features are obtained by increasing the spatial resolution from 2.0 mm to 1.0 mm. Results are consistent between left hemisphere (LH) and right hemisphere (RH). Results of three different imaging resolutions are shown: 2.0 mm (blue), 1.5 mm (green) and 1.0 mm (red). The vertices on the WGB surface are color-coded (left bottom) to illustrate: the gyral crowns (cyan), walls (gray), or fundi (yellow). A transition zone is seen from tangential (to the WGB) diffusion to radial at the depth of ~20% cortical thickness for voxels in the sulcal walls and fundi.

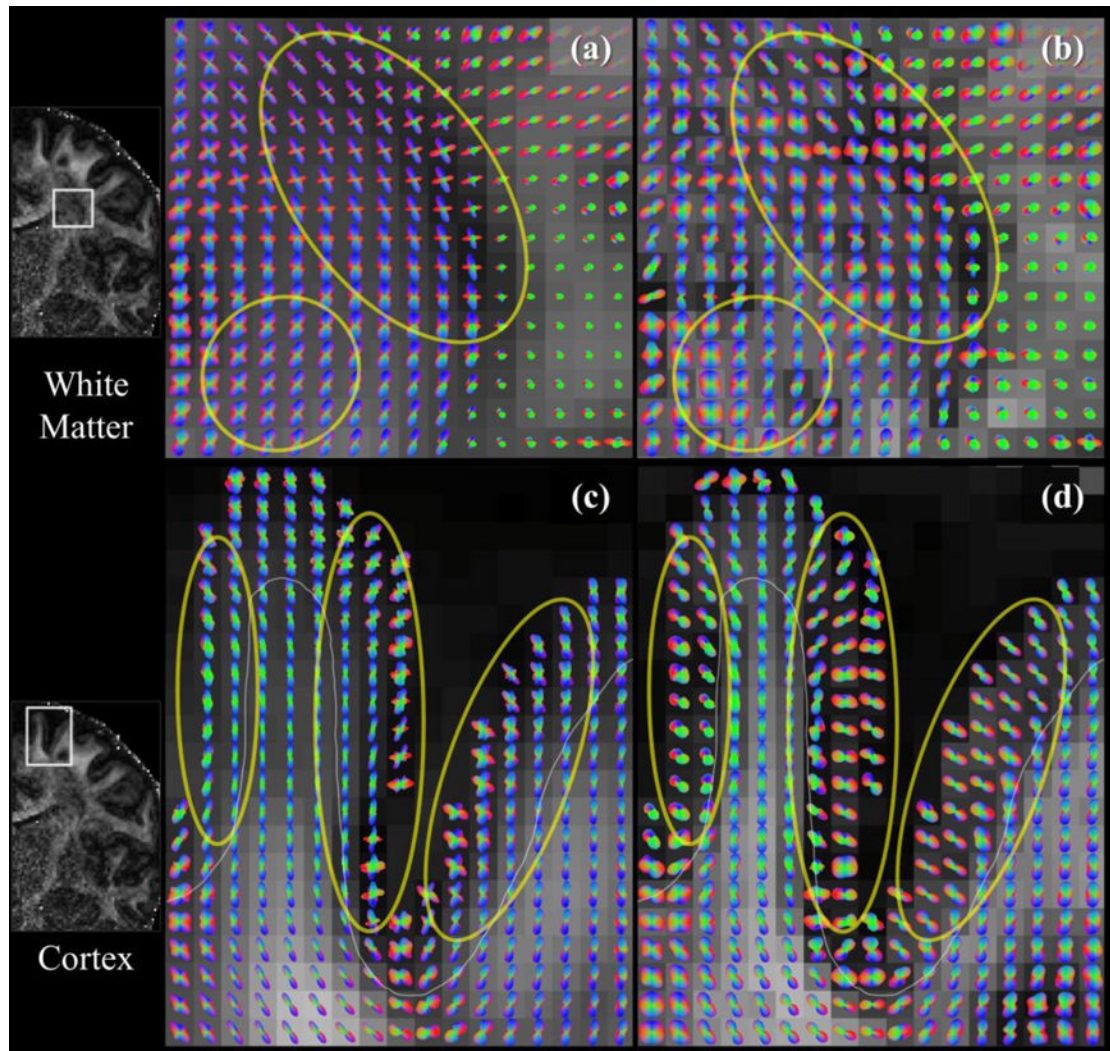


Figure 7. The q-ball ODFs of the two datasets. The crossing structures in WM are better revealed in (a) the 2.0 mm, $b=8k$ dataset than (b) the 1.0 mm, $b=1.5k$ dataset. In cortical GM, the partial voluming effect with WM is more prominent in (c) the 2.0 mm, $b=8k$ data than (d) the 1.0 mm, $b=1.5k$ dataset. The gray contour in panels c & d represents the WGB surface. The ODFs are max-min normalized to 0–1 to facilitate visualization.

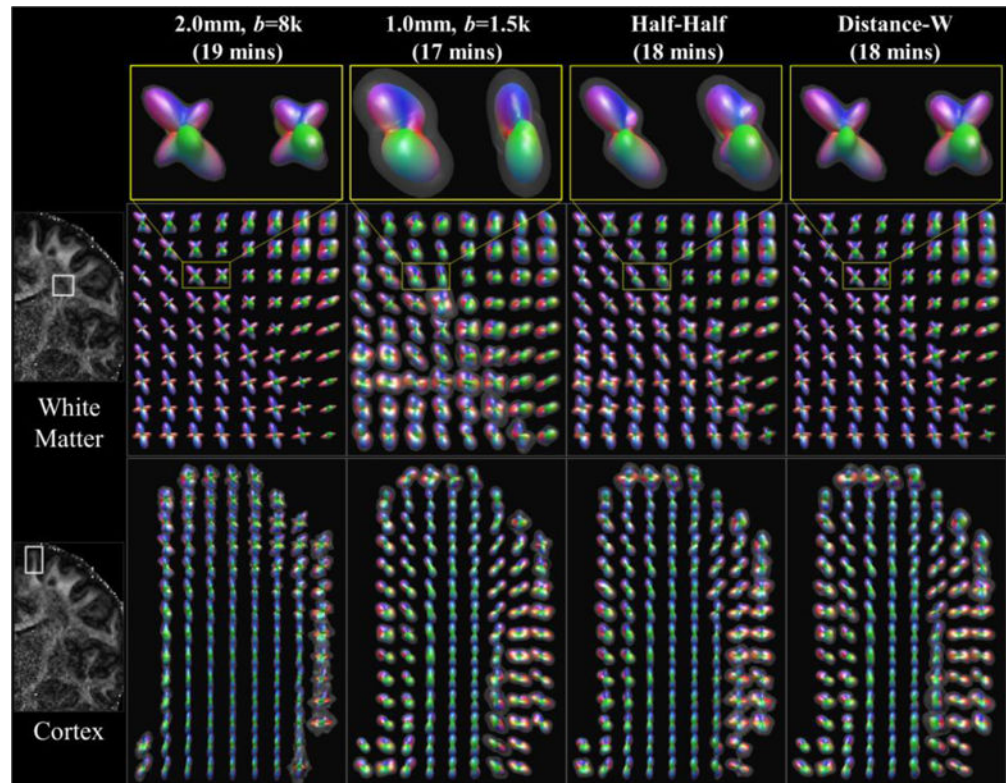


Figure 8.

The Jackknife resampling of q-ball ODFs. An ROI in centrum semiovale and cortical GM is zoomed in respectively, to exemplify the reliability across 200 Jackknife samples. The average ODFs (opaque) \pm 3 SDs (transparent) were shown. To facilitate visualization, the average ODFs are max-min normalized to 0–1. The Distance-W HIBRID dataset demonstrates reasonable reliability and preserves both of the angular and spatial resolution advantages in individual datasets.

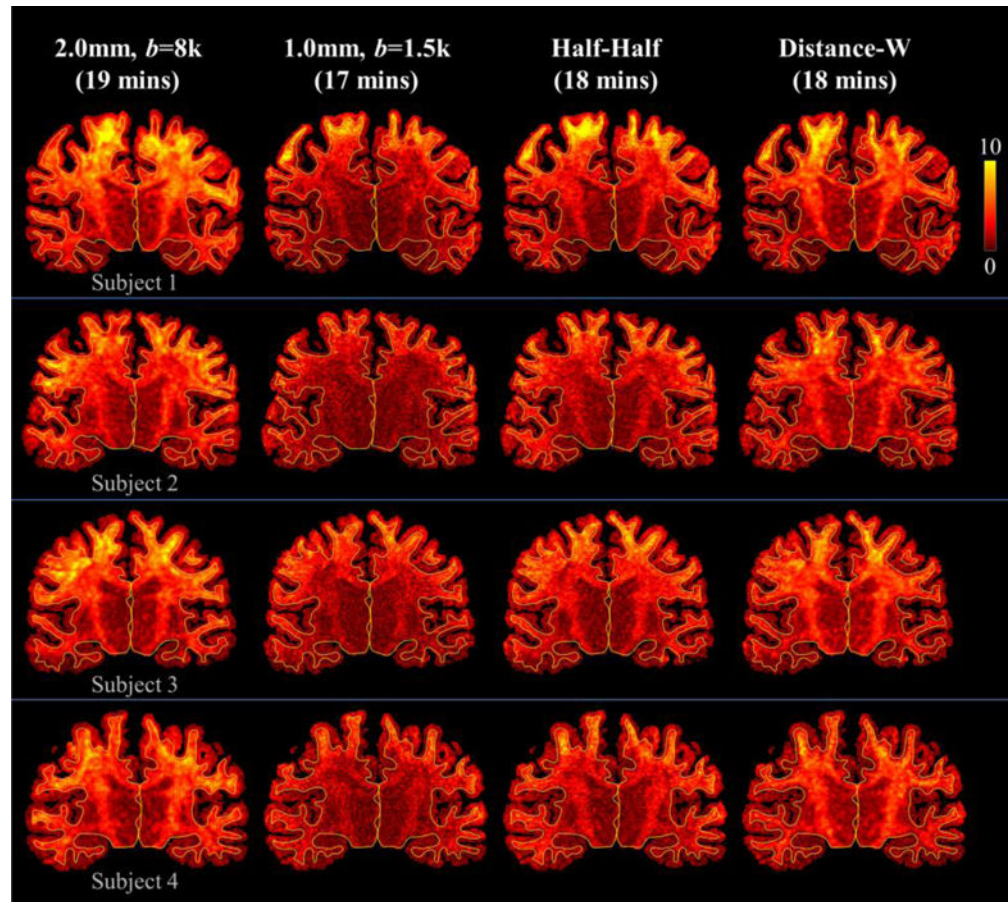


Figure 9.

The ODF CNR map based on Jackknife resampling on q-ball ODF. The yellow contour represents the WGB surface. Compared to the 2.0 mm, b=8k dataset, the Half-Half weighting somewhat deteriorates the CNR in WM. The HIBRID data using the Distance-W method largely retained the high CNR in the 2.0 mm, b=8k dataset.

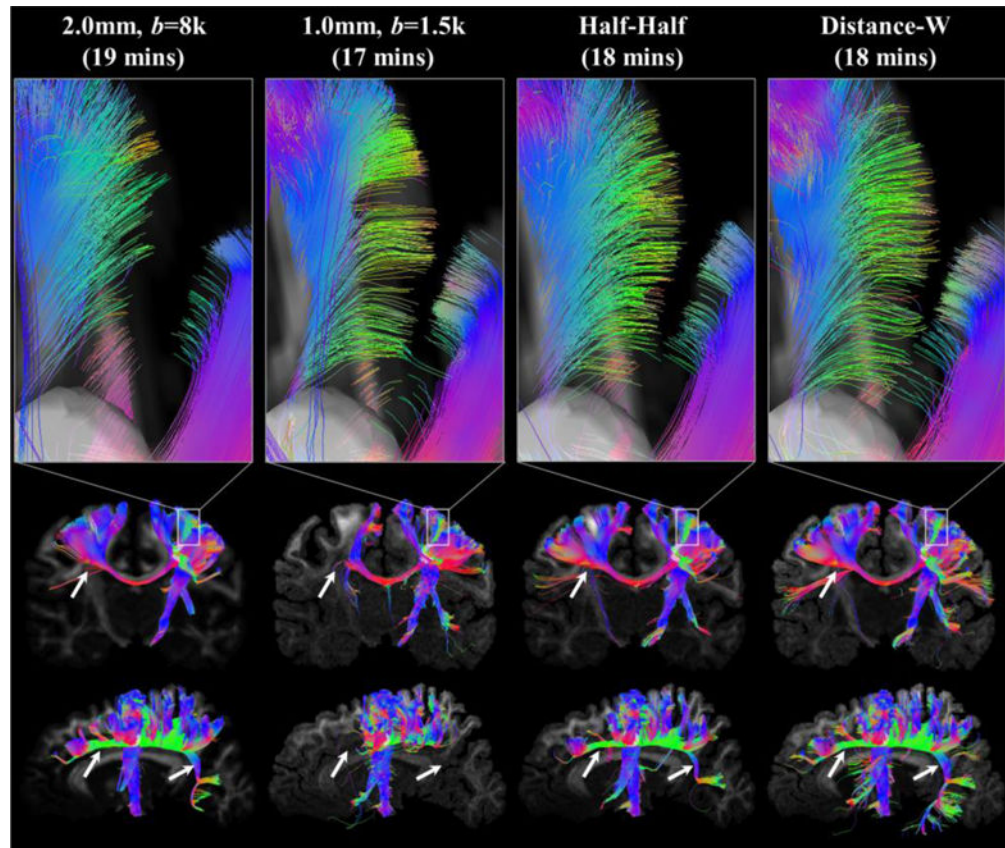


Figure 10. Streamline trajectories. In cortical GM, the streamlines proceed straight towards gyral crowns in the 2.0 mm, $b=8k$ dataset and do not bend towards gyral walls. In deep WM, some tracts fail to survive the fiber crossing regions in the 1.0 mm, $b=1.5k$ data. Both HIBRID datasets demonstrate the complementary benefits of high b -value and high spatial resolution compared to the two separate datasets alone. Overall, the Distance-W HIBRID data best represents the known microanatomy. The transparent white-color surface in the top row represents the spherical ROI.

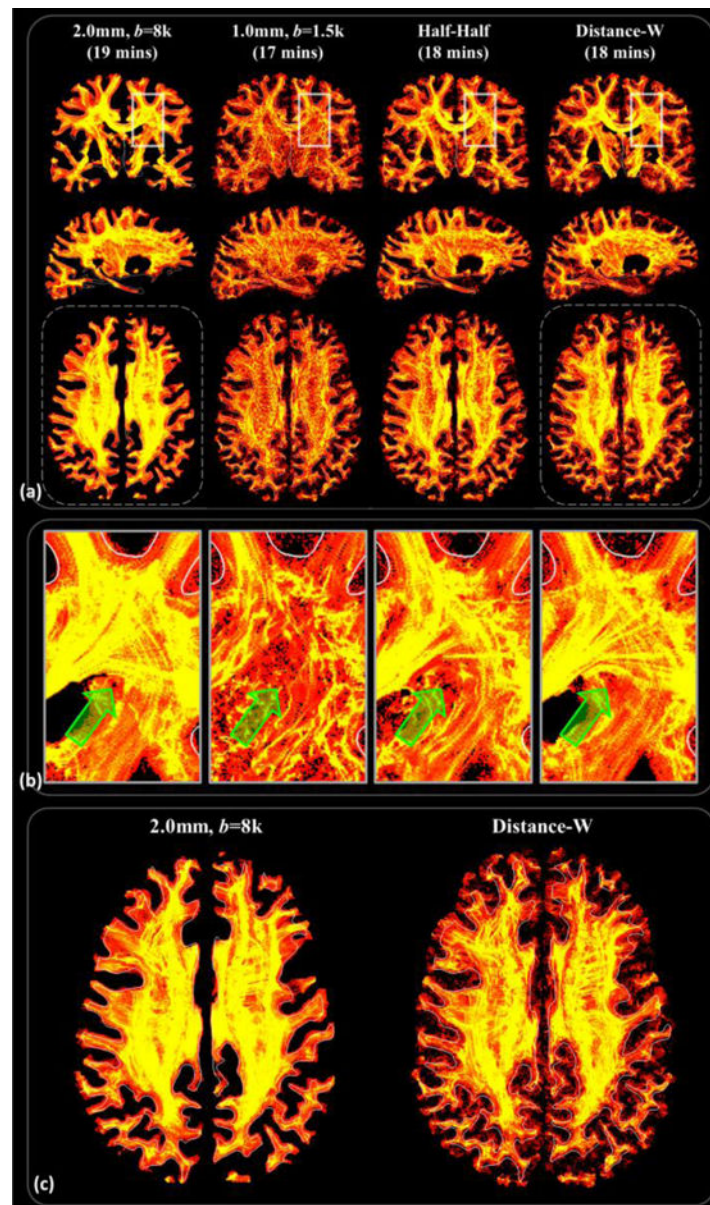


Figure 11.

TDI maps generated from the individual and combined datasets. (a) The TDI maps in three orthogonal views. (b) The 1.0 mm, $b=1.5k$ demonstrates a deficiency in recovering streamlines passing through centrum semiovale. Overall, the Distance-W HIBRID and the 2.0 mm, $b=8k$ datasets perform identically well in finding crossing structures in deep WM (b). Near cerebral cortex, the Distance-W HIBRID dataset reveals more streamlines that pass across the WGB and extend into cortical regions compared to the 2.0 mm, $b=8k$ dataset (c).